JOC The Journal of Organic Chemistry

pubs.acs.org/joc Article

Direct S_N2 or S_N2X Manifold—Mechanistic Study of Ion-Pair-Catalyzed Carbon(sp^3)–Carbon(sp^3) Bond Formation

Richmond Lee,* Chi Bong Eric Chao, Xu Ban, Siu Min Tan, Haibo Yu, Christopher J. T. Hyland, and Choon-Hong Tan

Cite This: J. Org. Chem. 2022, 87, 4029–4039 Read Online

ACCESS | Metrics & More | Article Recommendations | Supporting Information

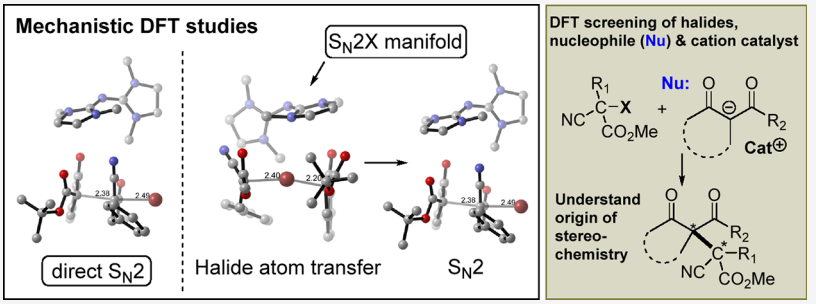

ABSTRACT: Density functional theory (DFT) is used in this work to predict the mechanism for constructing congested quaternary–quaternary carbon(sp^3)–carbon(sp^3) bonds in a pentanidium-catalyzed substitution reaction. Computational mechanistic studies were carried out to investigate the proposed S_N2X manifold, which consists of two primary elementary steps: halogen atom transfer (XAT) and subsequent S_N2. For the first calculated model on original experimental substrates, XAT reaction barriers were more kinetically competitive than an S_N2 pathway and connect to thermodynamically stable intermediates. Extensive computational screening modeling was then done on various substrate combinations designed to study the steric influence and to understand the mechanistic rationale, and calculations reveal that sterically congested substrates prefer the S_N2X manifold over S_N2. Different halides as leaving groups were also screened, and it was found that the reactivity increases in the order of I > Br > Cl > F, in agreement with the strength of C–X bonds. However, DFT modeling suggests that chlorides can be a viable substrate for the S_N2X process, which should be further explored experimentally. ONIOM calculations on the full catalyst model predicted the correct stereochemical outcome, and further catalyst screening with cationic Me_4N^+ and K^+ predicted that pentanidium is still the choice for S_N2X C–C bond formation.

INTRODUCTION

Substitution reactions are of fundamental importance to chemical synthesis and also occur in important biological processes. The common variants of the substitution mechanism are bimolecular nucleophilic substitution (S_N2), unimolecular nucleophilic substitution (S_N1), internal nucleophilic substitution (S_Ni), or as a continuum between S_N1 and S_N2,[1,2] and in depth basic understanding of substitution mechanism can reveal important insights into a reaction (Figure 1A).[3,4] In contrast to the well-established backside attack observed for S_N2 reactions, another possible S_N2 substitution mechanism involves frontside nucleophilic attack on the leaving group—a possibility not considered here due to steric hindrance.[5] Halogenophilic substitution (S_N2X) on the other hand is a less known process, and the mechanistic details of these processes are only just starting to be understood.[6,7] These distinct mechanistic differences between substitution reactions are depicted in Figure 1, whereby to distinguish these mechanistic variances solely by experimental data is not always possible. Therefore, computational mechanistic studies of the substitution mechanisms have been pivotal to enrich the understanding of these processes in both chemical and biological systems.[8]

An S_N2X process in chiral cationic pentanidium-catalyzed carbon–sulfur bond formation has been previously uncovered by our groups using density functional theory (DFT) and experimental techniques.[9] Recent progress on this topic predicted an S_N2X pathway occurring in the base-mediated isomerization of the halide substrate in relation to forming a chiral carbon–nitrogen bond through a proposed dynamic kinetic resolution model (Figure 1B).[10] These studies highlighted an important facet of substitution reactions

Received: November 15, 2021
Published: March 4, 2022

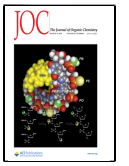

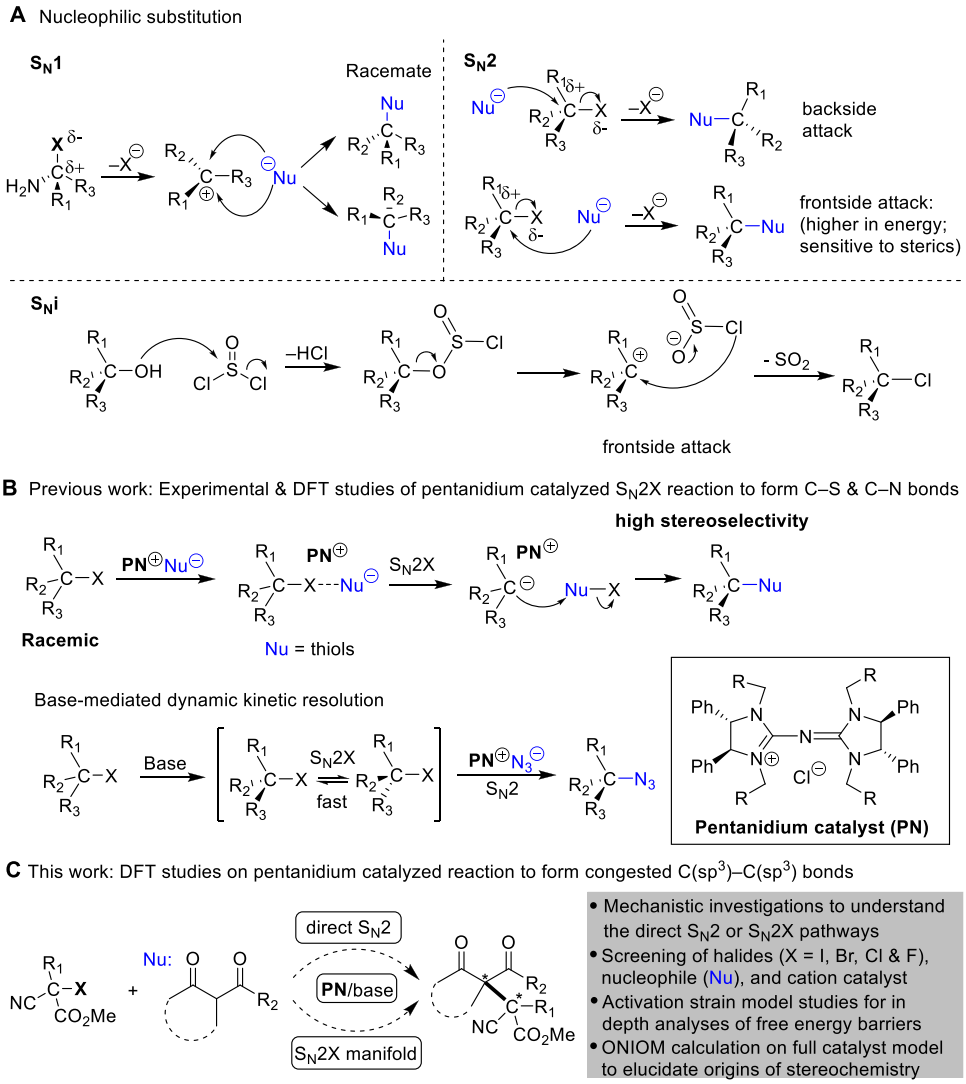

Figure 1. (A) Comparison of nucleophilic substitution variances, (B) previous work on S_N2X chemistry, and (C) objectives of this work.

operating *via* the less commonly explored S_N2X pathway toward forging highly desirable, but synthetically challenging carbon−heteroatom bonds. In these examples, both DFT and experimental studies played a synergistic and instrumental role in clarifying the reaction mechanism and chemical characteristics of S_N2X and enabled elegant reaction design strategies to achieve a library of difficult-to-make compounds.

Very recently, the experimental investigation of the halogenophilic substitution reaction with bromides catalyzed by pentanidium was further extended to highly challenging quaternary−tertiary or quaternary−quaternary carbon(sp^3)−carbon(sp^3) bond formation.[11,12] The halogenophilic substitution or S_N2X manifold proposed for this process is enantioconvergent, which leads to an interesting departure to the putative S_N1 or $S_{RN}1$ mechanism that is usually expected to operate for such sterically hindered substrates. In the context of this work, the S_N2X manifold consists of two primary elementary steps, which are halogen atom transfer (XAT) and S_N2. To fully understand the chemistry behind this intriguing substitution reaction involving vicinal quaternary carbon-(sp^3)−carbon(sp^3) bond formation, quantum chemical calculations were performed to predict and rationalize the S_N2 and S_N2X dichotomy (Figure 1C). To take a step further, DFT modeling was carried out to predict if chlorides and fluorides, which have stronger C−X bonds and are expected to be more challenging to activate, could undergo the S_N2X manifold. Finally, computational modeling of the full chiral catalyst model was carried out to rationalize the stereochemistry of this enantiospecific process. An initial version of this work was deposited in ChemRxiv on 15 November 2021 (reference: https://doi.org/10.26434/chemrxiv-2021-n9hrb).[13]

COMPUTATIONAL METHODS

Conformational Search and DFT Calculations. Grimme's CREST iMTD-GC algorithm,[14] combined with the extended semiempirical tight binding method GFN2-xTB,[15] was used to provide initial structural predictions of most stable conformers. Conformational search of ion pair complexes was carried out with the implicit solvent GFN2(ALPB) model with the toluene parameter in "NCI" mode. The most stable energy conformer ranked by energy was then further optimized with DFT and carried out with Gaussian 16 computational chemistry suite.[16] Gas-phase geometry optimization of minimum and transition state electronic structures was performed at this level of theory: Minnesota functional M11,[17] Pople's basis set 6-31G(d,p),[18] and Stuttgart-Dresden effective core potential (SDD) for Cs atom.[19,20] Frequency calculations were carried out at that level to ensure convergence—positive eigenvalues for minima and one single negative for saddle points—corrected with the quasi-harmonic

https://doi.org/10.1021/acs.joc.1c02782
J. Org. Chem. 2022, 87, 4029−4039

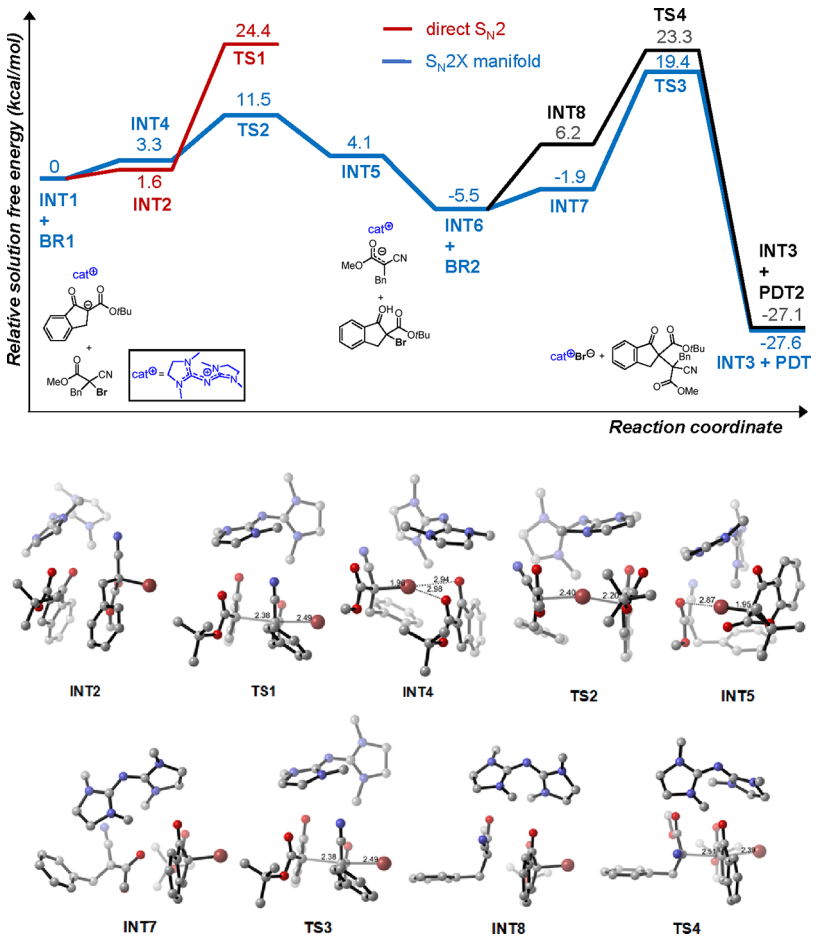

Figure 2. Relative solution free energy profile comparison of the one-step S_N2 (red) and S_N2X–S_N2 (blue/black) pathways (top) and 3-D structures of intermediates and transition states (bottom). DFT calculations at the M11/def2-TZVP/SMD(toluene)//M11/6-31G(d,p) level of theory and energy values are in kcal/mol. 3-D structures with H omitted for clarity are color-coded, representing C (gray), N (blue), O (red), and Br (brown) rendered by Cylview,[36] with key bond distances in Å.

approximated frequencies,[21] where frequencies <100 cm^{-1} were scaled to 100 cm^{-1}. Quasi-harmonic approximated thermochemical corrections and zero point vibrational energies were thus determined at the gas phase M11 functional level. Solution energies were considered with single-point calculations with the SMD model,[22] with toluene parameters on the gas-phase optimized structures at this level of theory: M11/def2-TZVP/SMD(toluene).[23,24] The M11/def2-TZVP/SMD(toluene) energies together with thermal and vibrational corrections based on gas-phase vibrations constitute the relative solution free energy, ΔG_{sol}, reported herein. The ΔG_{sol} is corrected to consider the passage of 1 atm gas into 1 M in solution, $\Delta G^{1atm\rightarrow 1M}$ as follows

$$\Delta G^{1atm\rightarrow 1M} = \Delta N \times RT\ln(RT/P)$$

where ΔN is the number of moles of gas change from the reactant to product and $RT\ln(RT/P)$ equals to 1.89 kcal/mol at 298 K.[25]

The distortion/interaction activation strain model was further used to understand and rationalize the reactivity of the S_N2X–S_N2 pathways with the gas-phase TS structures, molecular fragments, and optimized starting structures calculated at the M11/def2-TZVP level of theory.[26−31] Further calculations on benchmarking of theory, solvation model, and solvent screening and modeling of isomerization of the bromide with base can be found in the Supporting Information.

ONIOM Calculations for Full Catalyst Model. Gas-phase minimum or transition state electronic structure optimizations with the full catalyst model were carried out with ONIOM,[32] a two-layer integrated molecular orbital and molecular mechanics formalism. The molecular orbital calculation utilizes M11/6-31G(d,p), covering the catalyst core and substrates, while molecular mechanics utilizes semiempirical PM6,[33] covering the large aryl substituents of the catalyst (see Supporting Information). Frequency calculations were also done at the ONIOM(M11/6-31G(d,p):PM6) level of theory on the optimized structures. The electronic energies were improved with a higher-level single-point calculation at M11/def2-TZVP. The M11/def2-TZVP energies together with thermal and vibrational corrections based on gas-phase vibrations constitute the relative free energy, ΔG, reported here. Despite the lowering of computational costs with ONIOM, such methods provide reasonable geometries and the DFT single-point calculations at the M11/def2-TZVP level of theory will provide more accurate energies for the computational predictions.[10]

RESULTS AND DISCUSSION

Truncated Pentanidium and First Model. DFT calculations were performed to rationalize the mechanism of the quaternary C–C bond process with a truncated achiral pentanidium catalyst model (see Figure 2). Initial calculations involved modeling the molecular binding of bromide **BR1** to the catalyst–enolate complex **INT1**, which resulted in the formation of pre-S_N2 complex **INT2**, ΔG_{sol} = 1.6 kcal/mol with respect to **INT1** and **BR1**. The intermediate **INT2** is primed for direct substitution *via* the S_N2 pathway through transition state **TS1**, with a relative Gibbs free energy barrier of $\Delta G^{\ddagger}_{sol}$ = 24.4 kcal/mol with respect to **INT1** and **BR1**, generating the product **PDT** and the catalyst–bromide complex **INT3**. Another envisioned pathway proceeds *via* the

https://doi.org/10.1021/acs.joc.1c02782
J. Org. Chem. 2022, 87, 4029−4039

Table 1. Computational Screening of Bromo-, Chloro-, and Fluoro-Cyanoesters and Malonate Esters[a]

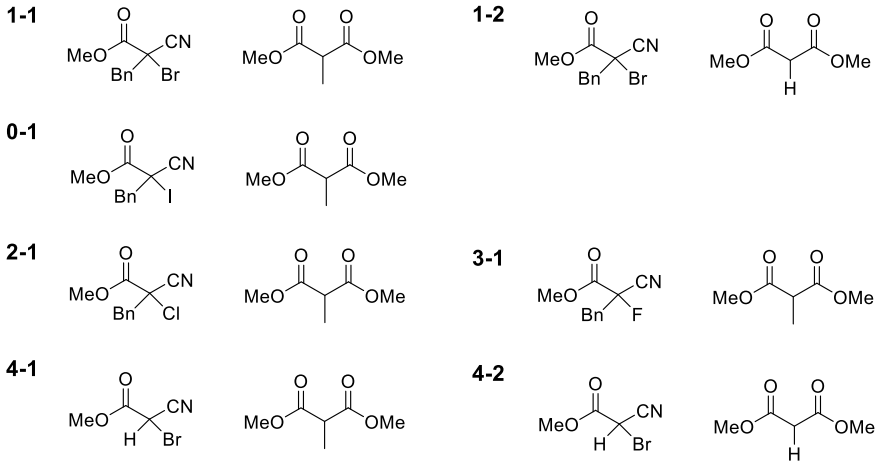

substrate set (#)	1-1	1-2	0-1	2-1	3-1	4-1	4-2
TS1_#	24.8	26.2	20.2	28.6	38.4	17.6	18.6
INT4_#	7.9	9.2	1.4	4.7	9.6	10.0	10.1
TS2_#	11.8	13.7	4.3	20.0	55.1	10.8[b]	12.1
INT6_# + X2_#	−9.5	−4.8	−8.3	−10.0	−10.0	−12.9	−8.2
TS3_#	13.8 (23.3)	15.0 (19.8)	11.9 (20.2)	17.7 (27.7)	28.6 (38.6)	11.3 (24.2)	11.8 (20.0)

[a]DFT calculations at the M11/def2-TZVP/SMD(toluene)//M11/6-31G(d,p) level of theory. Values are solution free energies in kcal/mol relative to respective **INT1** + **X1** (values in parenthesis are **TS3** solution free energies relative to **INT6** + **X2**). [b]Optimized to a minimum structure.

halogenophilic S_N2X manifold, starting with the pretransition intermediate **INT4** formed by the coordination between intermediate **INT1** and **BR1** (ΔG_{sol} = 3.3 kcal/mol), and is held together by halogen bonding between Br and the ketoester anion,[6,34,35] the key interaction, which predisposes the complex to undergo the halogen atom transfer (XAT) process. Subsequently, the halogen-bonded complex **INT4** undergoes bromine atom transfer from the ketoester *via* **TS2** (with the low energy barrier of $\Delta G^{\ddagger}_{sol}$ = 11.5 kcal/mol) to form a cyanoester bromide complex intermediate **INT5** (ΔG_{sol} = 4.1 kcal/mol). The dissociation of the cyanoester bromide **BR2** from the catalyst complex **INT6** is thermodynamically stable and exergonic (ΔG_{sol} = −5.5 kcal/mol). Therefore, we envisage an opportunity for the ketoester bromide **BR2** to undergo base isomerization and calculations revealed that this is energetically viable (see Supporting Information Scheme S1).

Binding of organo−bromide **BR2** and intermediate **INT6** with the C−Br bond facing away from the carbanion generates two possible intermediates **INT7** and **INT8**, leading to two diastereomers. **INT8** undergoes S_N2 displacement *via* transition state **TS4** (overall activation barrier of $\Delta G^{\ddagger}_{sol}$ = 28.8 kcal/mol with respect to **INT6** and **BR2**) to generate the diastereomer **PDT2** and pentanidium-Br salt **INT3** (ΔG_{sol} = −27.1 kcal/mol). The predicted major diastereomer **PDT** is generated from intermediate **INT7** through a more stable transition state **TS3**, with the overall solution free energy activation barrier of $\Delta G^{\ddagger}_{sol}$ = 24.9 kcal/mol with respect to **INT6** and **BR2**.

In summary, using the truncated catalyst model, DFT calculations predict a more energetically accessible pathway *via* the S_N2X instead of the direct S_N2 displacement, due to a more energetically competitive XAT process and the preferential thermodynamic stability of the **INT6** and **BR2** intermediates. At this point, the isomerization of the ketoester bromide **BR2** can occur, which allows for dynamic kinetic resolution in the chiral catalyst version, as suggested by previous DFT studies.[9,10]

Computational Screening of Electrophiles/Nucleophiles. Computational screening of various electrophiles and nucleophiles was carried out to predict reactivity and to further investigate the structure−electronic relation in the truncated pentanidium model. The first part involved replacing the cyclic ketoester nucleophile with the malonate ester (**1-1**), whereby the free energy barrier for the S_N2 pathway *via* **TS1_1-1** (see Table 1, $\Delta G^{\ddagger}_{sol}$ = 24.8 kcal/mol) was calculated to be nearly isoenergetic to the cyclic ketoester. For the S_N2X manifold, the first XAT step *via* **TS2_1-1** (see Table 1, $\Delta G^{\ddagger}_{sol}$ = 11.8 kcal/mol) is nearly isoenergetic to **TS2** but forms a very stable intermediate pair **INT6_1-1** and malonate ester bromide **BR2_1-1** (−9.5 kcal/mol relative to the starting species). The overall barrier for the concomitant S_N2 step **TS3_1-1**, $\Delta G^{\ddagger}_{sol}$ = 23.3 kcal/mol taken with reference to **INT6_1-1** and **BR2_1-1**, is 1.6 kcal/mol lower than that of the cyclic ketoester's second S_N2 free energy barrier of 24.9 kcal/mol. This difference can be rationalized by a less rigid nucleophile and as demonstrated by the comparison of the entropy component of $-T\Delta S^{\ddagger}_{sol}$ for **TS3_1-1** 7.9 versus **TS3** 12.9 kcal/mol at 298 K. The less rigid ketoester nucleophile has a lower entropy component by 5 kcal/mol and correspondingly lower $\Delta G^{\ddagger}_{sol}$.

Substituting the methyl group on the α-carbon of the malonate ester with hydrogen could effectively aid in mitigating the reaction barrier due to lowered steric repulsion between the substrates. The **1-2** substrate set (Table 1) was modeled, and calculations revealed that the direct S_N2 pathway barrier, **TS1_1-2**, at $\Delta G^{\ddagger}_{sol}$ = 26.2 kcal/mol is higher by 1.4 kcal/mol than that of **TS1_1-1**. The XAT barrier through **TS2_1-1** is also higher at 13.7 kcal/mol, and the intermediate pair **INT6_1-1** and **BR2_1-2** were calculated to be energetically less stable than **1-1** at −4.8 kcal/mol. The overall barrier for the S_N2 elementary step in the S_N2X manifold through **TS3_1-2** was calculated to be much more accessible at 19.8

https://doi.org/10.1021/acs.joc.1c02782
J. Org. Chem. 2022, 87, 4029−4039

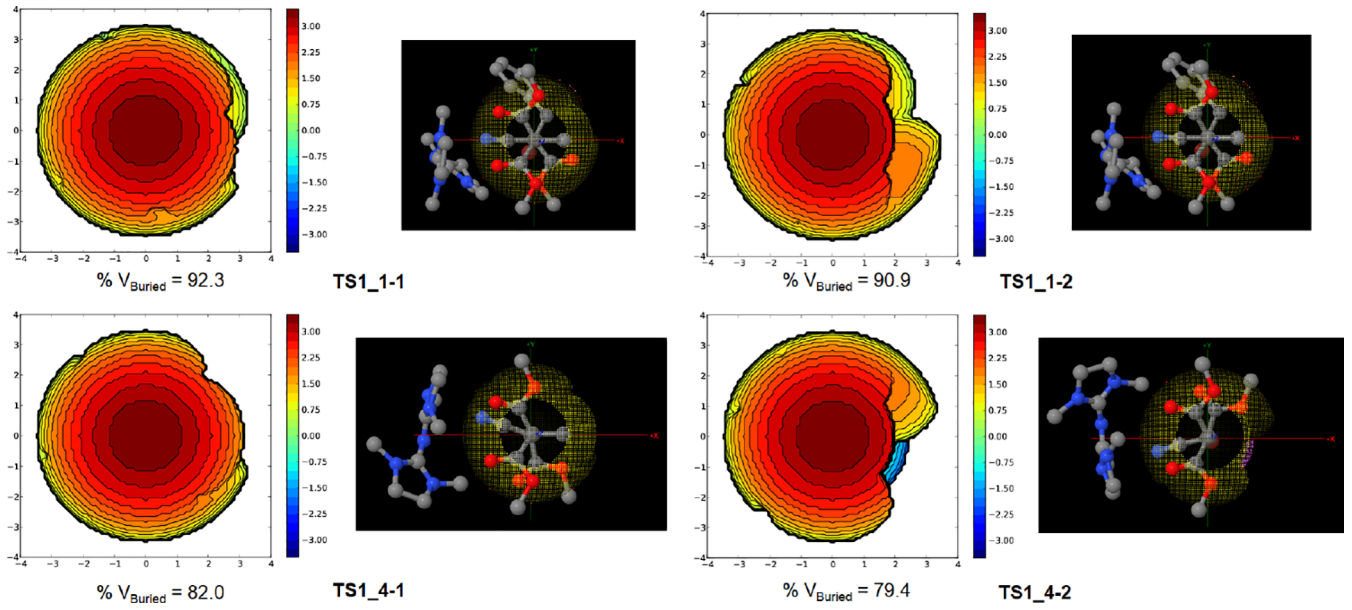

Figure 3. Buried volume plots of TS1 structures of **1-1**, **1-2**, **4-1**, and **4-1**. Isocontour steric map in Å—red for hindered and blue for less hindered regions. % V_{Buried} is the percentage buried volume based and centered on the cyanoester. Show in the left of the steric map are the corresponding molecular perspectives.

Table 2. Computational Screening of Chloro-Cyanoesters and Various Malonate Esters[a]

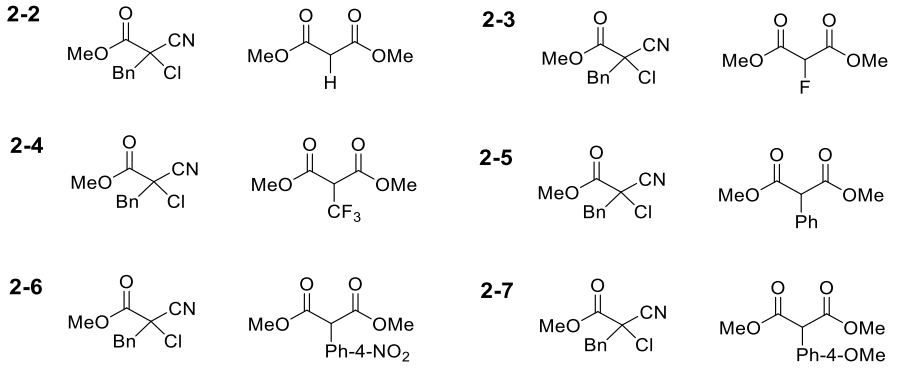

substrate set (#)	2-2	2-3	2-4	2-5	2-6	2-7
TS1_#	30.1	27.5	38.1	33.9	36.8	33.0
TS2_#	21.8	19.2	27.6	27.0	29.3	26.2
INT6_# + Cl2_#	−4.9	−7.2	4.7	−4.2	1.6	−5.6
TS3_#	19.1 (24.0)	17.1 (24.3)	43.2	27.7 (31.9)	32.0	25.8 (31.4)

[a]DFT calculations at the M11/def2-TZVP/SMD(toluene)//M11/6-31G(d,p) level of theory. Values are solution free energies in kcal/mol relative to **INT1** + **Cl1** (values in parenthesis are **TS3** solution free energies relative to **INT6** + **Cl2**).

kcal/mol due to the cyanoester carbanion attacking a less hindered sp^3 carbon. Further replacing the benzyl group with H on the cyanoester (**4-1** and **4-2**) lowered the **TS1** barrier significantly to about 18 kcal/mol on average. The **TS2** XAT barrier for **4-2** and estimated barrier for **4-1**, (no TS with imaginary frequency could be optimized for this structure), are 12.1 and 10.8 kcal/mol, respectively—which are close to **TS2_1-1** and **TS2_1-2**. The **TS3** barriers relative to **INT6** and **BR2** intermediate pairs are higher: 24.2 and 20.0 kcal/mol for **4-1** and **4-2**, respectively. This suggests that the less sterically bulky cyanoester bromide electrophile could steer the reaction pathway toward direct S_N2 for making quaternary−tertiary (**4-1**) and tertiary−tertiary (**4-2**) C−C bonds in the first instance. The corollary of a direct S_N2 is the negative impact on stereoconvergence, as the formation of the resting state **INT6** + **BR2** that is important for dynamic kinetic resolution *via* isomerization of **BR2** through **TS5** is restricted.

The SambVca code was used to qualitatively visualize the steric environment of the S_N2 **TS1** transition state structures of **1-1**, **1-2**, **4-1**, and **4-2** centered on the cyanoester (see Figure 3).[37] The buried volume plot shows that the more sterically congested substrates **1-1** and **1-2** have higher % of buried volume (91 to 92) directly translating to higher **TS1** activation barrier energies (~25 kcal/mol), compared to **4-1** and **4-2** (79 to 82%), which have a lower **TS1** barrier (~18 kcal/mol).

Next, the scope of the electrophiles was extended to include cyanoester iodine (**0-1**), chloride (**2-1**), and fluoride (**3-1**) (see Table 1). While the C−I bond is weaker, both C−Cl and C−F bonds are stronger than C−Br and might lead to lower or higher free energy barriers for the S_N2 or S_N2X processes

https://doi.org/10.1021/acs.joc.1c02782
J. Org. Chem. 2022, 87, 4029−4039

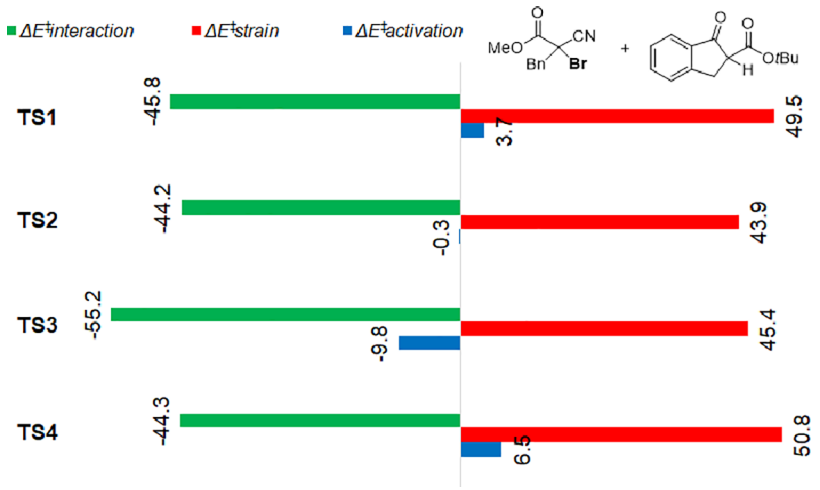

Figure 4. Distortion/interaction activation strain model for the first model. DFT calculations at the M11/def2-TZVP level of theory. Energy values are in kcal/mol.

Table 3. Free Energy Barrier, $\Delta G^{\ddagger}_{sol}$, and Distortion/Interaction Activation Strain Model Comparison for all Screened Substrates[a]

substrate set (#)	0-1	1-1	1-2	4-1	4-2	3-1	2-1	2-2	2-3	2-4	2-5	2-6	2-7	*R*
$\Delta G^{\ddagger}_{sol}$, **TS1_#**	20.2	24.8	26.2	17.6	18.6	38.4	28.6	30.1	27.5	38.1	33.9	36.8	33	
$\Delta E^{\ddagger}_{activation}$	−1.2	1.9	3.0	−0.7	−0.4	18.4	7.3	9.7	7.1	16.6	12.7	15.7	11.9	0.98
$\Delta E^{\ddagger}_{strain}$	46.9	50.0	50.2	48.1	45.2	80.1	59.6	57.5	57.1	71.7	70.0	71.1	69.6	0.95
$\Delta E^{\ddagger}_{interaction}$	−48.1	−48.1	−47.1	−48.7	−45.6	−61.7	−52.4	−47.8	−50.0	−55.1	−57.3	−55.3	−57.7	−0.83
$\Delta G^{\ddagger}_{sol}$, **TS2_#**	6.2	11.8	13.7	10.8	12.1	55.1	20.0	21.8	19.2	27.6	27.0	29.3	26.2	
$\Delta E^{\ddagger}_{activation}$	−14.6	−10.6	−8.6	−7.8	−8.8	33.5	−1.4	0.6	−2.6	5.1	2.9	5.9	2.4	0.99
$\Delta E^{\ddagger}_{strain}$	12.8	31.4	33.6	12.0	17.6	61.2	38.0	38.7	35.4	49.2	50.3	53.7	49.7	0.87
$\Delta E^{\ddagger}_{interaction}$	−27.4	−42.0	−42.2	−19.8	−26.5	−27.7	−39.3	−38.0	−38.0	−44.1	−47.5	−47.8	−47.4	−0.18
$\Delta G^{\ddagger}_{sol}$, **TS3_#**	22.1	23.3	19.7	24.2	20.0	38.6	27.7	24.1	24.4	42.9	31.8	32.0	31.4	
$\Delta E^{\ddagger}_{activation}$	−0.8	1.8	−1.3	2.3	0.4	18.6	7.5	4.8	5.1	18.6	11.2	8.9	10.5	0.98
$\Delta E^{\ddagger}_{strain}$	45.9	48.5	42.7	50.6	45.9	79.1	55.2	50.9	50.7	72.0	60.5	60.5	58.6	0.96
$\Delta E^{\ddagger}_{interaction}$	−46.8	−46.8	−43.9	−48.3	−45.4	−60.5	−47.7	−46.1	−45.6	−53.5	−49.2	−51.6	−48.1	−0.85

[a]Calculated at M11/def2-TZVP/SMD(toluene)//M11/6-31G(d,p) and activation strain model at the M11/def2-TZVP level of theory. Values are in kcal/mol. Pearson *R* coefficient (unitless) measures the correlation between $\Delta G^{\ddagger}_{sol}$ and the energy components of the activation strain model.

depending on the relative strength of the C−X bonds. As expected, the calculated barriers for direct S_N2 through **TS1_0-1** are lower at 20.2 kcal/mol (compared with **TS1_1-1** at 24.8 kcal/mol), but **TS1_2-1** is higher at 28.6 kcal/mol and even much higher for **TS1_3-1** at 38.4 kcal/mol. The free energy barriers for the XAT process for **0-1** is facile at only 4.3 kcal/mol, but both **2-1** and **3-1** increased in comparison to **1-1**. The **TS2_2-1** $\Delta G^{\ddagger}_{sol}$ at 20.0 kcal/mol, which is kinetically accessible, but **TS2_3-1** is prohibitively high at 55.1 kcal/mol. The rate-determining second S_N2 displacement process of the S_N2X manifold through **TS3_0-1**, **TS3_2-1,** and **TS3_3-1** were determined to be 20.2, 27.7, and 38.6 kcal/mol, respectively. Computational modeling suggests that it is energetically facile for iodide to easily undergo S_N2X, feasible for chloride but highly unlikely for fluoride.

Computational Screening of Chlorides. To computationally predict if chlorides can undergo the S_N2X manifold with reasonable energies, attention was next turned toward computational screening of cyanoester chloride with various malonate ester nucleophiles. Beginning with **2-2**, the calculated **TS1_2-2** and **TS2_2-2** $\Delta G^{\ddagger}_{sol}$ at 30.1 and 21.8 kcal/mol (see Table 2 entry **2-2**), relative to **INT1_2-2** and **Cl1_2-2,** respectively, are slightly higher than **2-1**. As the **INT6_2-2** and **Cl2_2-2** energies become less exergonic or less stable, the activation barrier for **TS3_2-2** with $\Delta G^{\ddagger}_{sol}$ = 25.0 kcal/mol relative to **INT6_2-2** and **Cl2_2-2** decreases. Substituting hydrogen with electronegative fluorine (**2-3**) results in stabilized **TS1_2-3**, **TS2_2-3,** and **TS3_2-3** energies at 27.5, 19.2, and 17.1 kcal/mol relative to **INT1_2-3** and **Cl1_2-3,** respectively; the overall barrier for **TS3_2-3** improved to 24.3 kcal/mol with respect to **INT6_2-3** and **Cl2_2-3**. However, the presence of highly electron-withdrawing but bulky $-CF_3$ group (**2-4**) increases the barriers significantly to 38.1, 27.6, and 43.2 kcal/mol for **TS1_2-4**, **TS2_2-4,** and **TS3_2-4**, respectively. Having phenyl substituents on the malonate ester gave higher calculated barriers compared to others (see Table 2 entries **2-5**, **2-6,** and **2-7**). Computational modeling revealed that the presence of the electron-withdrawing group ($-NO_2$) on the phenyl para position (**2-6**) raises the barrier for XAT, **TS2_2-6** with 29.3 kcal/mol due to a less reactive anion toward abstracting Cl, whereas species containing electron-donating −OMe (**2-7**) moiety enhances nucleophilicity and lowers barrier for XAT.

Distortion/Interaction Activation Strain Model Analyses. To further dissect the energies qualitatively and examine the mechanistic preference of the examples vide supra, as well as rationalize the competition between diastereomeric **TS3** and **TS4**, distortion/interaction activation strain modeling was

https://doi.org/10.1021/acs.joc.1c02782
J. Org. Chem. 2022, 87, 4029−4039

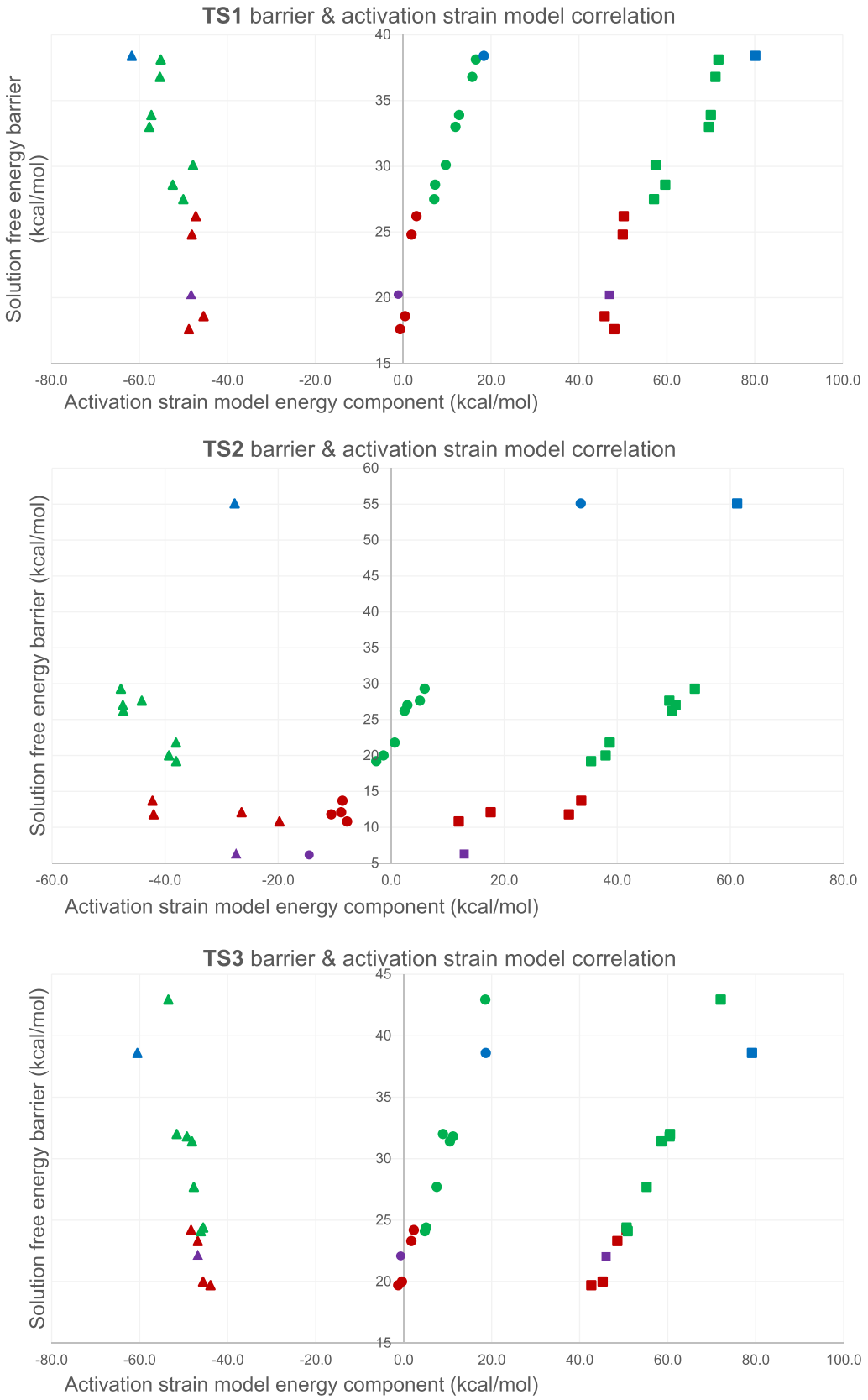

Figure 5. Charts of **TS1**, **TS2**, and **TS3** $\Delta G^{\ddagger}_{sol}$ vs individual energy component of the activation strain model. Circle (●) represents $\Delta E^{\ddagger}_{activation}$, square (■) for $\Delta E^{\ddagger}_{strain}$, and triangle (▲) for $\Delta E^{\ddagger}_{interaction}$. Colors are used to represent the halides: iodide (purple), bromide (red), chloride (green), and fluoride (blue).

carried out (see Figure 4).[27] The activation strain model revealed higher strain energy, $\Delta E^{\ddagger}_{strain}$, for **TS1** (50.8 kcal/mol) as a result of unfavorable geometry distortion in the transition state, followed by **TS3** (43.9 kcal/mol) and **TS4** (49.5 kcal/

https://doi.org/10.1021/acs.joc.1c02782
J. Org. Chem. 2022, 87, 4029−4039

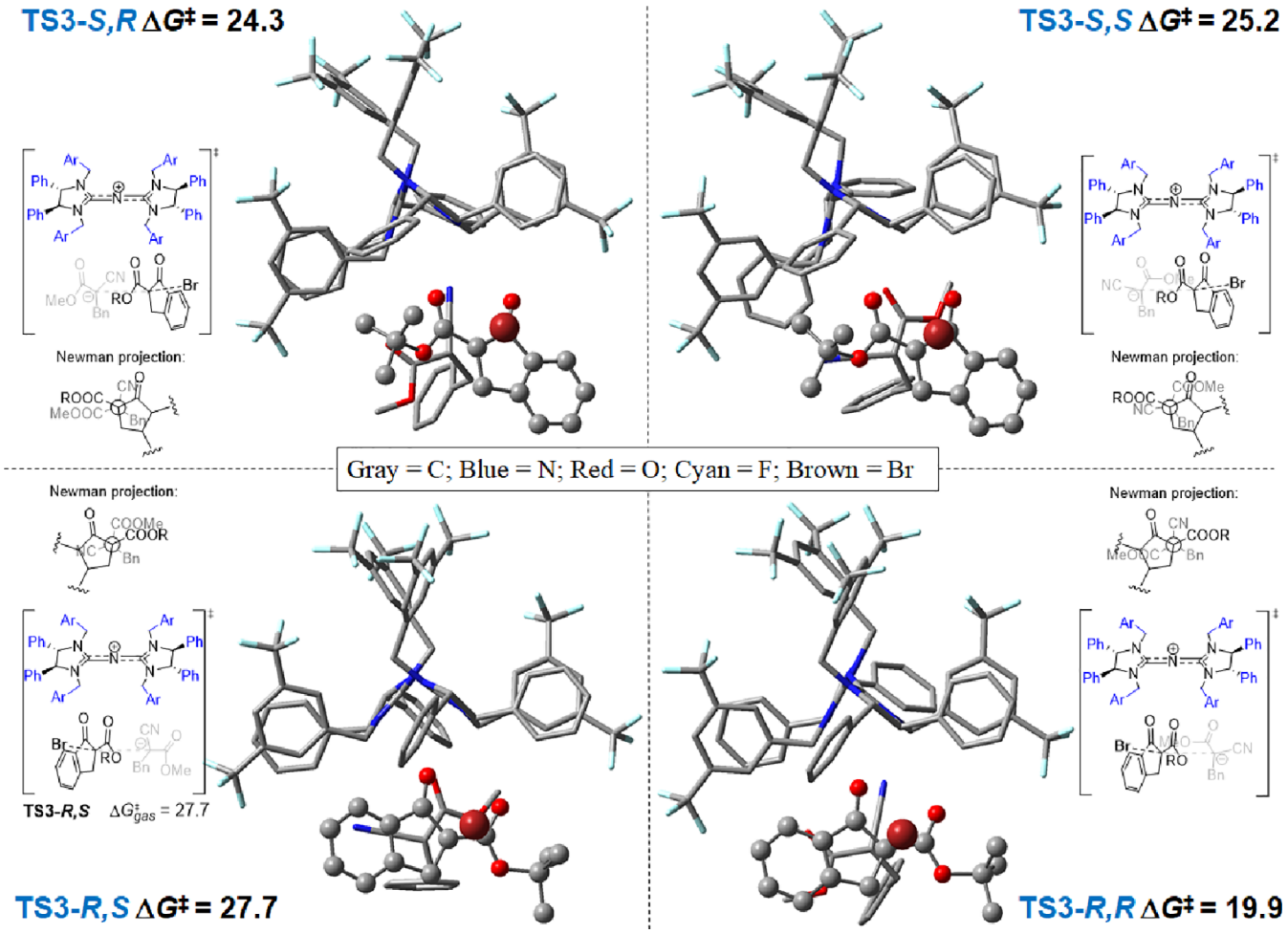

Figure 6. Computational stereochemical prediction for C−C bond formation with the full catalyst model. ONIOM M11/def2-TZVP//M11/6-31G(d,p):PM6 level of theory. Free energy values are in kcal/mol.

mol). The activation energy $\Delta E^{\ddagger}_{\text{activation}}$ follows a similar trend, with **TS3** having the smaller $\Delta E^{\ddagger}_{\text{activation}}$ than **TS1** or **TS4**. These energies suggest that through **TS1** or the direct S_N2 process, the nucleophilic approach by the ketoester carbanion toward the cyanoester bromide is not ideal, which results in the strain energy $\Delta E^{\ddagger}_{\text{strain}}$ for **TS1** to be much higher than **TS3** or **TS4**. Diastereoselection could be controlled by the second displacement step of the S_N2X manifold through **TS3** and **TS4**. The more stable transition state **TS3** has a significantly lower $\Delta E^{\ddagger}_{\text{strain}}$ than **TS4**, suggesting less geometry distortion as the electron-rich −CN group in **TS3** pivots toward the cationic pentanidium catalyst (Figure 4). For the XAT **TS2**, the stronger dipole interaction energy compensates the strain component, resulting in negative $\Delta E^{\ddagger}_{\text{activation}}$ at −9.8 kcal/mol.

Activation strain energies for the rest of computationally screened substrates in Tables 1 and 2 are summarized in Table 3 with the Pearson correlation coefficient and plotted in Figure 5. This allows for appraisal of the free energy barriers with the activation strain model and predicts if there are any important correlations relating to reactivity and the component $\Delta E^{\ddagger}_{\text{activation}}$, $\Delta E^{\ddagger}_{\text{strain}}$ and $\Delta E^{\ddagger}_{\text{interaction}}$. Comparing the direct S_N2 energies for the bromides, ranked from highest to lowest (Table 1)—**TS1_1-2** ($\Delta G^{\ddagger}_{\text{sol}}$ = 26.2 kcal/mol), **TS1_1-1** (24.8 kcal/mol), **TS1_4-2** (18.6 kcal/mol), and **TS1_4-1** (17.6 kcal/mol)—the activation strain model $\Delta E^{\ddagger}_{\text{activation}}$ follows a similar trend (3.0, 1.9, 0.4, and −0.7 kcal/mol), with the direct S_N2 energy barriers becoming favourable as the bromide becomes unencumbered. As such, the direct S_N2 pathway becomes more accessible with the secondary halide, while quaternary−quaternary C−C bond formation favors the S_N2X manifold. Based on this understanding, it is suggested that under higher reaction temperature, the direct S_N2 route could become thermodynamically competitive, despite the XAT step having a lower free energy barrier and a much higher second S_N2 free energy barrier for the less sterically impeded **4-1** and **4-2** (**TS3** free energy barrier of 24.2 and 20.0 kcal/mol relative to **INT6** + **BR2**, respectively).

Across the halides (Table 3: **0-1**, **1-1**, **2-1**, and **3-1**), the S_N2 transition states—**TS1** and **TS3**—$\Delta E^{\ddagger}_{\text{activation}}$ and $\Delta E^{\ddagger}_{\text{strain}}$ increase with a significant jump for fluoride **3-1**. **TS1** and **TS3** $\Delta E^{\ddagger}_{\text{strain}}$ also increase from iodide to fluoride, which correlates to the higher energy cost required to break increasingly stronger C-X bonds, despite having a more negative $\Delta E^{\ddagger}_{\text{interaction}}$. The halide series also shows that the **TS1** $\Delta E^{\ddagger}_{\text{activation}}$ becomes more negative, while **TS2** $\Delta E^{\ddagger}_{\text{activation}}$ becomes more positive, resulting in direct S_N2 becoming more competitive. Similarly, **TS2** $\Delta E^{\ddagger}_{\text{strain}}$ becomes more positive across the series, which correlates to increase in their free energy barriers. It is also noteworthy that **TS2_2-1** has negative $\Delta E^{\ddagger}_{\text{activation}}$ of −1.4 kcal/mol, indicating that it is plausible for chloride to undergo S_N2X, vide supra. For fluoride **3-1**, a much higher $\Delta G^{\ddagger}_{\text{sol}}$ for **TS2** as compared to **TS1** could

https://doi.org/10.1021/acs.joc.1c02782
J. Org. Chem. 2022, 87, 4029−4039

Table 4. - Computational Screening of Me_4N^+ and K^+ as Cationic Catalysts[a]

substrate set (#)	INT2_#	TS1_#	INT4_#	TS2_#	INT6_# + X2_#	INT7_#	TS3_#
1-1	5.5	24.8	7.9	11.8	−9.5	−1.0	13.8
2-1	5.2	28.6	4.7	20.0	−10.0	−3.4	15.0
1-1_Me_4N^+	−4.4	11.5	−5.1	−2.8	−21.9	−16.7	2.3
2-1_Me_4N^+	4.3	25.4	3.2	15.5	−12.6	−6.9	16.2
1-1_K^+	−7.1	10.9	−9.3	−6.0	−15.9	−20.1	1.8
2-1_K^+	2.0	24.8	−0.1	11.9	−6.6	−10.2	15.8

[a]DFT calculations at the M11/def2-TZVP/SMD(toluene)//M11/6-31G(d,p) level of theory. Values are solution free energies in kcal/mol relative to **INT1** + **X1**.

be correlated to the $\Delta E^{\ddagger}_{activation}$, that is −27.7 and −61.7 kcal/mol, respectively, which could be attributed to a weaker $\sigma^*(C^-\cdots F)$ interaction.

From Figure 5, the $\Delta E^{\ddagger}_{strain}$ for **TS1** averages 20 kcal/mol for I, 48 kcal/mol for Br, 65 kcal/mol for Cl, and 80 kcal/mol for F, and $\Delta E^{\ddagger}_{interaction}$ averages −48 kcal/mol for I, −48 kcal/mol for Br, −53 kcal/mol for Cl, and −62 kcal/mol for F. The trend for **TS2** is expected to be the same as **TS1**, with I having the lowest barrier of 20 kcal/mol and $\Delta E^{\ddagger}_{activation}$ of −14.6 kcal/mol, followed by Br (10 to 12 kcal/mol) and $\Delta E^{\ddagger}_{activation}$ within −10 to −9 kcal/mol. Next is Cl, where **TS2** free energy barrier ranges from 20 to 30 kcal/mol and $\Delta E^{\ddagger}_{activation}$ within −1 to 6 kcal/mol. Not surprisingly, F has the highest energy barrier and $\Delta E^{\ddagger}_{activation}$. The $\Delta E^{\ddagger}_{strain}$ for **TS2** averages 13 kcal/mol for I, 24 kcal/mol for Br, 45 kcal/mol for Cl, and 61 kcal/mol for F, and $\Delta E^{\ddagger}_{interaction}$ averages −27 kcal/mol for I, −33 kcal/mol for Br, −43 kcal/mol for Cl, and −28 kcal/mol for F. For **TS3**, the barrier for I is 22.1 kcal/mol and $\Delta E^{\ddagger}_{activation}$ is −0.8 kcal/mol. Br **TS3** $\Delta G^{\ddagger}_{sol}$ ranges from 20 to 25 kcal/mol and $\Delta E^{\ddagger}_{activation}$ ranges from −1 to 2 kcal/mol; Cl has a barrier of 24 to 43 kcal/mol and $\Delta E^{\ddagger}_{activation}$ from 5 to 19 kcal/mol; F has a barrier of 39 kcal/mol and $\Delta E^{\ddagger}_{activation}$ of 19 kcal/mol. The $\Delta E^{\ddagger}_{strain}$ for **TS3** averages 46 kcal/mol for I, 47 kcal/mol for Br, 59 kcal/mol for Cl, and 79 kcal/mol for F, and $\Delta E^{\ddagger}_{interaction}$ averages −47 kcal/mol for I, −46 kcal/mol for Br, −49 kcal/mol for Cl, and −61 kcal/mol for F. Analysis of the activation barrier and activation strain model in Table 3 and Figure 4 reveals strong correlation between the ease for X leaving group and C−X bond strength (I > Br > Cl > F) to decreasing average **TS** free energy barrier and $\Delta E^{\ddagger}_{activation}$ in general (I < Br < Cl < F). Higher average $\Delta E^{\ddagger}_{strain}$ also resulted in higher **TS** barriers, indicating that $\Delta E^{\ddagger}_{strain}$ and $\Delta E^{\ddagger}_{activation}$ are highly correlated to $\Delta G^{\ddagger}_{sol}$ (R = 0.87 to 0.96). However, $\Delta E^{\ddagger}_{interaction}$ showed a less impact on both barrier and $\Delta E^{\ddagger}_{activation}$, suggesting weaker correlation (R = −0.85 to −0.18).

Full Catalyst Model (ONIOM). In order to probe the origin of stereochemistry in the asymmetric version of pentanidium-catalyzed carbon−carbon bond formation, ONIOM calculations (see Computational Methods), at the M11/def2-TZVP//M11/6-31G(d,p):PM6 level of theory, were performed for the full catalytic model.

The truncated pentanidium DFT model suggests that the rate-determining and enantio-determining step is the second S_N2 substitution in the S_N2X manifold, after **INT6** and **BR2**. As such, the ONIOM model will focus on the **TS3** free energies for the four different stereochemical outcomes shown in Figure 6, with the transition state **TS3-*R,R*** ($\Delta G^{\ddagger}$ = 19.9 kcal/mol) being the most stable, followed by **TS3-*S,R*** (24.3 kcal/mol), **TS3-*S,S*** (25.2 kcal/mol), and **TS3-*S,R*** (27.7 kcal/mol). More information about the pre-TS complexes can be found in the Supporting Information. The predicted stereochemistry of the major product corroborates the absolution configuration of the product, determined by single-crystal X-ray diffraction data.[11]

Further analysis of the transition state structures (Figure 6) revealed that the most optimal geometry of the nucleophile, when bound to the catalyst, occurs when the cyano group pivots toward the pentanidium moiety, generating the most stable transition state **TS3-*R,R*** and second most stable **TS3-*S,R***. In short, the pentanidium binds more favorably when the negatively charged cyano group is closer *via* electrostatic attraction in the ion pair and predisposes the nucleophile in a reorientation. This stereochemical preference is further distinguished between **TS3-*R,R*** and **TS3-*S,R*** when the cyclic ketoester halide approaches toward the reoriented nucleophile, with the benzyl in a preferentially unhindered position, affording the experimentally obtained *R,R* product. Because the *R*-configuration **BR2** is transformed to minor *S,R* product via **TS3-*S,R*** (second lowest barrier), *S*-**BR2** transformed to major *R,R* product *via* **TS3-*R,R*** (lowest) is predicted to be dominant and faster, resulting in isomerization from *R*-**BR2** to *S*-**BR2**.

Cationic Catalyst Effects. A simple ammonium Me_4N^+ and potassium ion K^+ in place of the truncated pentanidium catalyst were used to further model the S_N2 and S_N2X reactions, in a bid to understand the catalyst influence on the mechanistic outcomes (see Table 4). The calculated direct S_N2 barrier for **1-1** substrates with ammonium and potassium cations gave lower free energy barriers (**TS1_1-1_Me_4N^+**, 15.9 and **TS1_1-1_K^+**, 18.0 kcal/mol relative to **INT2**) compared to pentanidium **1-1**. The XAT free energy barriers for Me_4N^+ and K^+ were also determined to be small—2.3 and 3.3 kcal/mol relative to **INT4**, respectively, leading to energetically stable **INT6** and **X2** intermediates (−21.9 and −15.9 kcal/mol, respectively). The free energy barrier for the subsequent substitution step in the S_N2X manifold (**TS3_1-1_Me_4N^+**, 24.2 kcal/mol relative to **INT6** and **X2** and **TS3_1-1_K^+**, 21.9 kcal/mol relative to **INT7**) was calculated to be higher than **TS1**'s barrier, which suggests that the direct S_N2 is more competitive, but S_N2X may still proceed coupled with the fact that the XAT barrier is low, and the **INT6** and **X2** intermediates formed after are highly exergonic.

To predict the viability of chlorides for S_N2X with ammonium and potassium cations, the chloride substrate set **2-1** was also modeled. Not surprising, the S_N2 barrier for the chlorides **TS1_2-1_Me_4N^+** and **TS1_2-1_K^+** are much higher than the bromides (25.4 and 24.8 kcal/mol, respectively). For XAT **TS2_2-1_Me_4N^+** and **TS2_2-1_K^+**, the free energy barriers are 15.5 and 12.0 kcal/mol, respectively, but are still much lower than S_N2. The second substitution **TS3_2-1_Me_4N^+** and **TS3_2-1_K^+** are 28.8 kcal/mol relative to **INT6** and **X2** and 26.0 kcal/mol relative to **INT7**, respectively,

https://doi.org/10.1021/acs.joc.1c02782
J. Org. Chem. 2022, 87, 4029−4039

which suggests that the direct S_N2 is more competitive. Like in the bromide scenario, that is, lower XAT barrier and stable intermediates formed after, it can be envisaged that S_N2X could operate competitively together with S_N2. Because modeling of both Me_4N^+ and K^+ showed that both S_N2 and S_N2X pathways are comparable for C−C bond formation, it would suggest that the pentanidium cation is more selective and preferentially drives the reaction toward S_N2X manifold, as the direct S_N2 is energetically less accessible.

CONCLUSIONS

In conclusion, the DFT model suggests that the reaction mechanism for the pentanidium-catalyzed construction of the sterically congested vicinal quaternary $C(sp^3)-C(sp^3)$ bond proceeds *via* a halogenophilic S_N2X manifold. In a bid to rationalize the mechanistic dichotomy between direct S_N2 or S_N2X process, computational screening of cyanoester and malonates with their derivatives of varying steric bulkiness showed that the direct S_N2 could be favored if the cyanoester bromide was less sterically demanding. Generally, the calculations predict that the S_N2X manifold's **TS2** (XAT) activation free energy barriers are more accessible and lower for the bromides and chlorides than **TS1** (S_N2), and the thermodynamic stability of the intermediates **INT6** and **BR2** or **Cl2** in the presence of base allows for the dynamic interconversion of the halides to be feasible. This in turn affords the high enantioselectivity through dynamic kinetic resolution concordant with previous reports.[9,10]

These theoretical calculations thus corroborate to the observed experimental data,[11] which represents a successful example of a S_N2X substitution reaction in assembling highly desirable yet synthetically challenging congested $C(sp^3)-C(sp^3)$ bond and offers guidance to predicting the optimal choice of reaction conditions or substrates. The plausible scope of bromides is further extended, as computationally screening of various halides also helped predict the suitability of chlorides for the S_N2X, for which the experimental work is currently ongoing. While the computational data presented here only described a single reaction system, the mechanistic insights into the halogenophilic S_N2X manifold can be used as a platform to develop reaction design strategies to afford other synthetically challenging molecules. To this end, further experimental and computational studies on harnessing and discovering other S_N2X reactivities are currently underway.

ASSOCIATED CONTENT

Supporting Information

The Supporting Information is available free of charge at https://pubs.acs.org/doi/10.1021/acs.joc.1c02782.

Benchmarking studies and other computational data, table summary of energies of optimized electronic structures, and XYZ coordinates (PDF)

AUTHOR INFORMATION

Corresponding Author

Richmond Lee − *School of Chemistry and Molecular Bioscience, University of Wollongong, Wollongong, NSW 2522, Australia; Molecular Horizons, University of Wollongong, Wollongong, NSW 2522, Australia;* orcid.org/0000-0003-1264-4914; Email: richmond_lee@uow.edu.au

Authors

Chi Bong Eric Chao − *School of Chemistry and Molecular Bioscience, University of Wollongong, Wollongong, NSW 2522, Australia; Molecular Horizons, University of Wollongong, Wollongong, NSW 2522, Australia*

Xu Ban − *Division of Chemistry and Biological Chemistry, Nanyang Technological University, 637371, Singapore*

Siu Min Tan − *Singapore University of Technology and Design, 487372, Singapore*

Haibo Yu − *School of Chemistry and Molecular Bioscience, University of Wollongong, Wollongong, NSW 2522, Australia; Molecular Horizons, University of Wollongong, Wollongong, NSW 2522, Australia;* orcid.org/0000-0002-1099-2803

Christopher J. T. Hyland − *School of Chemistry and Molecular Bioscience, University of Wollongong, Wollongong, NSW 2522, Australia; Molecular Horizons, University of Wollongong, Wollongong, NSW 2522, Australia*

Choon-Hong Tan − *Division of Chemistry and Biological Chemistry, Nanyang Technological University, 637371, Singapore;* orcid.org/0000-0003-3190-7855

Complete contact information is available at: https://pubs.acs.org/10.1021/acs.joc.1c02782

Notes

The authors declare no competing financial interest.

ACKNOWLEDGMENTS

We gratefully acknowledge financial support from the Australian Research Council (DE210100053, R.L.), UOW RITA Grant 2021 (H.Y. and R.L.), and a UOW Vice Chancellor's Research Fellowship (R.L.). We would also like to acknowledge Nanyang Technological University for Tier 1 grants (RG1/19 and RG2/20) and Ministry of Education (Singapore) Tier 2 grants (MOE2019-T2-1-091, C.H.T.). Computational resources are provided by the National Computing Infrastructure (Australia) through the Merit Allocation (NCMAS) and UOW Partnership Schemes. We would like to thank Dr. Davin Tan for helpful discussions.

REFERENCES

(1) Adero, P. O.; Amarasekara, H.; Wen, P.; Bohé, L.; Crich, D. The Experimental Evidence in Support of Glycosylation Mechanisms at the S_N1-S_N2 Interface. *Chem. Rev.* **2018**, *118*, 8242−8284.

(2) Hughes, E. D.; Ingold, C. K.; Whitfield, I. C. The Walden Inversion in the Replacement of Hydroxyl by Halogen. *Nature* **1941**, *147*, 206−207.

(3) Otto, R.; Brox, J.; Trippel, S.; Stei, M.; Best, T.; Wester, R. Single Solvent Molecules Can Affect the Dynamics of Substitution Reactions. *Nat. Chem.* **2012**, *4*, 534−538.

(4) Stei, M.; Carrascosa, E.; Kainz, M. A.; Kelkar, A. H.; Meyer, J.; Szabó, I.; Czakó, G.; Wester, R. Influence of the Leaving Group on the Dynamics of a Gas-Phase SN2 Reaction. *Nat. Chem.* **2016**, *8*, 151−156.

(5) Bento, A. P.; Bickelhaupt, F. M. Nucleophilicity and Leaving-Group Ability in Frontside and Backside S_N2 Reactions. *J. Org. Chem.* **2008**, *73*, 7290−7299.

(6) Sutar, R. L.; Huber, S. M. Catalysis of Organic Reactions through Halogen Bonding. *ACS Catal.* **2019**, *9*, 9622−9639.

(7) Zefirov, N. S.; Makhon'kov, D. I. X-Philic Reactions. *Chem. Rev.* **1982**, *82*, 615−624.

(8) Fu, Y.; Bernasconi, L.; Liu, P. Ab Initio Molecular Dynamics Simulations of the S_N1/S_N2 Mechanistic Continuum in Glycosylation Reactions. *J. Am. Chem. Soc.* **2021**, *143*, 1577−1589.

(9) Zhang, X.; Ren, J.; Tan, S. M.; Tan, D.; Lee, R.; Tan, C.-H. An Enantioconvergent Halogenophilic Nucleophilic Substitution (S_N2X) Reaction. *Science* **2019**, *363*, 400−404.
(10) Ren, J.; Ban, X.; Zhang, X.; Tan, S. M.; Lee, R.; Tan, C. H. Kinetic and Dynamic Kinetic Resolution of Racemic Tertiary Bromides by Pentanidium-Catalyzed Phase-Transfer Azidation. *Angew. Chem., Int. Ed.* **2020**, *59*, 9055−9058.
(11) Ban, X.; Fan, Y.; Kha, T.-K.; Lee, R.; Kee, C. W.; Jiang, Z.; Tan, C.-H. Pentanidium-Catalyzed Direct Assembly of Vicinal All-Carbon Quaternary Stereocenters through $C(Sp^3)$-$C(Sp^3)$ Bond Formation. *CCS Chem.* **2021**, *3*, 2192.
(12) Zhang, X.; Tan, C.-H. Stereospecific and Stereoconvergent Nucleophilic Substitution Reactions at Tertiary Carbon Centers. *Chem* **2021**, *7*, 1451−1486.
(13) Lee, R.; Chao, C. B. E.; Ban, X.; Tan, S. M.; Yu, H.; Hyland, C. J. T.; Tan, C.-H. Direct SN2 or SN2X Manifold − Mechanistic Study of Ion-Pair Catalyzed Carbon(Sp3)-Carbon(Sp3) Bond Formation; preprint. *ChemRxiv* **2021**, DOI: 10.26434/chemrxiv-2021-n9hrb.
(14) Pracht, P.; Bohle, F.; Grimme, S. Automated Exploration of the Low-Energy Chemical Space with Fast Quantum Chemical Methods. *Phys. Chem. Chem. Phys.* **2020**, *22*, 7169−7192.
(15) Bannwarth, C.; Ehlert, S.; Grimme, S. GFN2-XTB—An Accurate and Broadly Parametrized Self-Consistent Tight-Binding Quantum Chemical Method with Multipole Electrostatics and Density-Dependent Dispersion Contributions. *J. Chem. Theory Comput.* **2019**, *15*, 1652−1671.
(16) Frisch, M. J.; Trucks, G. W.; Schlegel, H. B.; Scuseria, G. E.; Robb, M. A.; Cheeseman, J. R.; Scalmani, G.; Barone, V.; Petersson, G. A.; Nakatsuji, H.; Li, X.; Caricato, M.; Marenich, A. V.; Bloino, J.; Janesko, B. G.; Gomperts, R.; Mennucci, B.; Hratchian, H. P.; Ortiz, J. V.; Izmaylov, A. F.; Sonnenberg, J. L.; Williams-Young, D.; Ding, F.; Lipparini, F.; Egidi, F.; Goings, J.; Peng, B.; Petrone, A.; Henderson, T.; Ranasinghe, D.; Zakrzewski, V. G.; Gao, J.; Rega, N.; Zheng, G.; Liang, W.; Hada, M.; Ehara, M.; Toyota, K.; Fukuda, R.; Hasegawa, J.; Ishida, M.; Nakajima, T.; Honda, Y.; Kitao, O.; Nakai, H.; Vreven, T.; Throssell, K.; Montgomery, J. A., Jr.; Peralta, J. E.; Ogliaro, F.; Bearpark, M. J.; Heyd, J. J.; Brothers, E. N.; Kudin, K. N.; Staroverov, V. N.; Keith, T. A.; Kobayashi, R.; Normand, J.; Raghavachari, K.; Rendell, A. P.; Burant, J. C.; Iyengar, S. S.; Tomasi, J.; Cossi, M.; Millam, J. M.; Klene, M.; Adamo, C.; Cammi, R.; Ochterski, J. W.; Martin, R. L.; Morokuma, K.; Farkas, O.; Foresman, J. B.; Fox, D. J. *Gaussian 16*, Revision A.03, 2016.
(17) Peverati, R.; Truhlar, D. G. Improving the Accuracy of Hybrid Meta-GGA Density Functionals by Range Separation. *J. Phys. Chem. Lett.* **2011**, *2*, 2810−2817.
(18) Ditchfield, R.; Hehre, W. J.; Pople, J. A. Self-Consistent Molecular-Orbital Methods. IX. An Extended Gaussian-Type Basis for Molecular-Orbital Studies of Organic Molecules. *J. Chem. Phys.* **1971**, *54*, 724−728.
(19) Bergner, A.; Dolg, M.; Küchle, W.; Stoll, H.; Preuß, H. Ab Initio Energy-Adjusted Pseudopotentials for Elements of Groups 13−17. *Mol. Phys.* **1993**, *80*, 1431−1441.
(20) Dolg, M.; Wedig, U.; Stoll, H.; Preuss, H. Energy-adjusted abinitio Pseudopotentials for the First Row Transition Elements. *J. Chem. Phys.* **1987**, *86*, 866−872.
(21) Ribeiro, R. F.; Marenich, A. V.; Cramer, C. J.; Truhlar, D. G. Use of Solution-Phase Vibrational Frequencies in Continuum Models for the Free Energy of Solvation. *J. Phys. Chem. B* **2011**, *115*, 14556−14562.
(22) Marenich, A. V.; Cramer, C. J.; Truhlar, D. G. Universal Solvation Model Based on Solute Electron Density and on a Continuum Model of the Solvent Defined by the Bulk Dielectric Constant and Atomic Surface Tensions. *J. Phys. Chem. B* **2009**, *113*, 6378−6396.
(23) Weigend, F. Accurate Coulomb-Fitting Basis Sets for H to Rn. *Phys. Chem. Chem. Phys.* **2006**, *8*, 1057.
(24) Weigend, F.; Ahlrichs, R. Balanced Basis Sets of Split Valence, Triple Zeta Valence and Quadruple Zeta Valence Quality for H to Rn: Design and Assessment of Accuracy. *Phys. Chem. Chem. Phys.* **2005**, *7*, 3297.
(25) Ho, J.; Klamt, A.; Coote, M. L. Comment on the Correct Use of Continuum Solvent Models. *J. Phys. Chem. A* **2010**, *114*, 13442−13444.
(26) Levandowski, B. J.; Hamlin, T. A.; Bickelhaupt, F. M.; Houk, K. N. Role of Orbital Interactions and Activation Strain (Distortion Energies) on Reactivities in the Normal and Inverse Electron-Demand Cycloadditions of Strained and Unstrained Cycloalkenes. *J. Org. Chem.* **2017**, *82*, 8668−8675.
(27) Bickelhaupt, F. M.; Houk, K. N. Analyzing Reaction Rates with the Distortion/Interaction-Activation Strain Model. *Angew. Chem., Int. Ed.* **2017**, *56*, 10070−10086.
(28) Wolters, L. P.; Bickelhaupt, F. M. The Activation Strain Model and Molecular Orbital Theory: Activation Strain Model and Molecular Orbital Theory. *Wiley Interdiscip. Rev.: Comput. Mol. Sci.* **2015**, *5*, 324−343.
(29) van Zeist, W.-J.; Bickelhaupt, F. M. The Activation Strain Model of Chemical Reactivity. *Org. Biomol. Chem.* **2010**, *8*, 3118.
(30) Legault, C. Y.; Garcia, Y.; Merlic, C. A.; Houk, K. N. Origin of Regioselectivity in Palladium-Catalyzed Cross-Coupling Reactions of Polyhalogenated Heterocycles. *J. Am. Chem. Soc.* **2007**, *129*, 12664−12665.
(31) Bickelhaupt, F. M. Understanding Reactivity with Kohn-Sham Molecular Orbital Theory: E2-SN2 Mechanistic Spectrum and Other Concepts. *J. Comput. Chem.* **1999**, *20*, 114−128.
(32) Vreven, T.; Morokuma, K.; Farkas, Ö.; Schlegel, H. B.; Frisch, M. J. Geometry Optimization with QM/MM, ONIOM, and Other Combined Methods. I. Microiterations and Constraints. *J. Comput. Chem.* **2003**, *24*, 760−769.
(33) Stewart, J. J. P. Optimization of Parameters for Semiempirical Methods V: Modification of NDDO Approximations and Application to 70 Elements. *J. Mol. Model.* **2007**, *13*, 1173−1213.
(34) Yang, H.; Wong, M. W. Application of Halogen Bonding to Organocatalysis: A Theoretical Perspective. *Molecules* **2020**, *25*, 1045.
(35) Cavallo, G.; Metrangolo, P.; Milani, R.; Pilati, T.; Priimagi, A.; Resnati, G.; Terraneo, G. The Halogen Bond. *Chem. Rev.* **2016**, *116*, 2478−2601.
(36) Legault, C. Y. *CYLview, 1.0b*; Université de Sherbrooke, 2009.
(37) Falivene, L.; Cao, Z.; Petta, A.; Serra, L.; Poater, A.; Oliva, R.; Scarano, V.; Cavallo, L. Towards the Online Computer-Aided Design of Catalytic Pockets. *Nat. Chem.* **2019**, *11*, 872−879.

https://doi.org/10.1021/acs.joc.1c02782
J. Org. Chem. 2022, 87, 4029−4039